

Model Order Reduction for Steady Aerodynamics of High-Lift Configurations

Alexander Vendl, Heike Faßbender

Technische Universität Braunschweig

Institut *Computational Mathematics*, AG Numerik

Fallersleber-Tor-Wall 23

38100 Braunschweig, Germany

a.vendl, h.fassbender@tu-braunschweig.de

Stefan Görtz, Ralf Zimmermann*, Michael Mifsud

German Aerospace Center (DLR)

Institute of Aerodynamics and Flow Technology

Lilienthalplatz 7

38108 Braunschweig, Germany

Stefan.Goertz@dlr.de, ralf.zimmermann@tu-braunschweig.de, michaelmifsud19@hotmail.com

April 22, 2013

Abstract

In aerodynamic applications many model reduction methods use Proper Orthogonal Decomposition (POD). In this work a POD-based method, called Missing Point Estimation (MPE), is modified and applied to steady-state flows with variation of the angle of attack. The main idea of MPE is to select a subset of the computational grid points (control volumes) and to limit the governing equations to these. Subsequently, the limited equations are projected onto the POD subspace. This approach has the advantage that the nonlinear right hand side of the governing equations has to be evaluated only for a small number of points (control volumes) in contrast to POD, for which the full right-hand side has to be evaluated. An error estimation for MPE in the continuous ODE setting is tackled. Numerical results are presented for the Navier-Stokes equations for two different industrially relevant, two-element high-lift airfoils, one which is normally adopted during landing and the other during take-off.

Keywords: Model Order Reduction, Missing Point Estimation, Proper Orthogonal Decomposition, CFD, Steady Aerodynamics

1 Introduction

In fluid dynamics reduced order models are often obtained via Proper Orthogonal Decomposition. Proper Orthogonal Decomposition, abbreviated by POD, is a technique to find a low-dimensional subspace which is capable of accurately representing solutions of the governing equations. Since the dimension of the POD subspace is typically very small compared to the high-dimensional solution space of the governing equations, low order surrogate models can be constructed. These so-called reduced order models can be solved more efficiently than the original high-dimensional model due to their low order.

*Present address: Technische Universität Braunschweig, Institut *Computational Mathematics*, AG Numerik, Fallersleber-Tor-Wall 23, 38100 Braunschweig, Germany

A frequently used technique for constructing reduced order models is projecting the governing equations onto a low-dimensional subspace. Often the POD subspace itself is chosen as the space onto which the equations are projected. In this case the projection is called Galerkin projection. While in many publications in context of fluid dynamics (e.g. [1]) the Galerkin projection is realized on the continuous governing equations, in the subspace projection method [2, 3] the projection is realized on the spatially discretized equations.

Assume that the spatially discretized governing equations are of the form $\frac{d\mathbf{w}(t)}{dt} = \mathbf{f}(\mathbf{w}(t))$, where $\mathbf{w} \in \mathbb{R}^{\mu N}$ is the flow solution and $\mathbf{f} \in \mathbb{R}^{\mu N}$ is the right hand side of the system. Then in the subspace projection method the reduced order model is given by

$$\frac{d\mathbf{a}(t)}{dt} = \Phi^T \mathbf{f}(\Phi \mathbf{a}(t)), \quad (1)$$

where $\Phi \in \mathbb{R}^{\mu N \times m}$ is the so-called POD basis matrix, which is orthogonal and consists of the m basis vectors spanning the POD subspace, and $\mathbf{a}(t) \in \mathbb{R}^m$ is the vector of suitable coefficients for these basis vectors. The reduced order solutions are thus given by $\mathbf{w}(t) = \Phi \mathbf{a}(t)$. However, since the reduced model contains the full order residual \mathbf{f} , there is a dependence on the degrees of freedom of the original model.

In order to alleviate this disadvantage of the subspace projection method, an alternative approach is presented in this work which aims at evaluating only some components of the right hand side \mathbf{f} , that is, taking into account only a subset of the governing equations at some computational grid points. This idea is based on the Missing Point Estimation (MPE) method, which has been introduced by Astrid [4] and has since been applied to heat transfer processes [5], electrical circuit modeling [6], and oil reservoir simulation [7]. The authors are not aware of any other applications of MPE to aerodynamics, other than their own publications [8, 9, 10].

We will consider steady, subsonic flows around two industrially relevant different, two-element high-lift airfoils, one which is normally adopted during landing and the other during take-off. The modeling and the CFD computations are based on previous work by the German Aerospace Center (DLR) and are not focussed on in this work which concentrates solely on appropriate model order reduction techniques. Since steady, subsonic flows are (mainly) elliptic in nature [11, Chapter 1], they are particularly suitable for applying Missing Point Estimation. This is due to the fact that for elliptic partial differential equations any point of the computational domain influences every other point.

Besides MPE, other techniques in the field of nonlinear model order reduction are the empirical interpolation [12, 13, 14, 15] and least-squares approximation [16] of nonlinear functions. Furthermore, in [17] the hyperreduction method is proposed, which is mathematically equivalent to MPE. Note that the Discrete Empirical Interpolation Method (DEIM) [14], which is one of the alternatives to MPE, cannot be applied as easily as MPE for the industrial problem considered here. This has to do with its idea to generate a second POD basis for the right hand side \mathbf{f} . For the steady-state solution the right hand side is equal to $\mathbf{0}$. In [14] the right hand side is split into a linear and a nonlinear terms. The second POD basis is then computed only for the nonlinear term. This procedure is not appropriate here, as it implies an intrusion into the (industrial) CFD code used. In the industrial problems considered here this was not possible.

The paper is organized as follows. First of all, the governing equations and POD are reviewed in Sections 2 and 3. Special focus on POD will be given to its numerical implementation of discretized flows. Section 4 then outlines MPE in context of aerodynamics and includes a subsection discussing a proposal on how to select a good subset of components of the right hand side \mathbf{f} to be evaluated for the CFD application considered. Moreover, following the ideas in [18], error estimation for MPE in continuous ODE setting is considered. Finally, in the last section MPE is applied to two high-lift configurations: one under take-off and the other one under landing conditions.

2 The Governing Equations

We will consider the Navier-Stokes equations - or more precisely the Reynolds-Averaged Navier-Stokes (RANS) equations. Let ρ , v_x , v_z , and E represent the flow field variables density, velocity components (for the horizontal and vertical Cartesian coordinates x and z), and total energy, respectively. The governing equations in conservative form are given by

$$\int_{\Omega} \frac{\partial \mathbf{W}}{\partial t} d\Omega + \oint_S \mathbf{F} \cdot \mathbf{n} dS = 0, \quad (2)$$

where

$$\mathbf{W}^T = (\rho, \rho v_x, \rho v_z, \rho E) \quad (3)$$

is the vector of the conservative variable. Ω stands for an arbitrary control volume with the boundary $S = \partial\Omega$. Finally, the flux vector \mathbf{F} represents the fluxes through the boundaries of the control volume. For more details on the definition of the flux vector, the reader is referred to [19, Chapter 2].

Additional equations are needed to model the turbulence. Here the Spalart-Allmaras one-equation turbulence model [19, Subsection 7.2.1] is considered. It uses a transport equation for an eddy-viscosity variable $\tilde{\nu}$ and can be written in integral form as

$$\int_{\Omega} \frac{\partial \tilde{\nu}}{\partial t} d\Omega + \oint_S F_T \cdot \mathbf{n} dS = \int_{\Omega} Q_T d\Omega, \quad (4)$$

where F_T denotes the flux and Q the source term; see [19, p. 240] for details.

The equations (2) and (4) are complemented by initial conditions describing the initial state of the flow, farfield boundary conditions and boundary conditions at the surface of the body under consideration.

Employing the method of lines, equations (2) and (4) are spatially discretized. A cell-vertex finite volume method is used with dual control volumes. In particular, the domain Ω is partitioned into N discrete control volumes Ω_i . The spatial discretization results in a set of ordinary differential equations of the form

$$\frac{d\mathbf{w}(t; \alpha)}{dt} = -\tilde{V}^{-1} \mathbf{R}(\mathbf{w}(t; \alpha)). \quad (5)$$

The angle of attack α enters the equations in the (farfield) boundary conditions.

The vector \mathbf{w} describes the discretized conservative variables as well as the eddy-viscosity variable $\tilde{\nu}$. It is collected such that each variable appears blockwise, that is

$$\mathbf{w}^T = (\boldsymbol{\rho}^T, \boldsymbol{\rho} v_x^T, \boldsymbol{\rho} v_z^T, \boldsymbol{\rho} E^T, \tilde{\nu}^T) \in \mathbb{R}^{5N}. \quad (6)$$

where each of the entries $\boldsymbol{\rho}$, $\boldsymbol{\rho} v_x$, $\boldsymbol{\rho} v_z$, and $\boldsymbol{\rho} E$ is a discretization of the corresponding function stored in a vector of size N . The residual vector $\mathbf{R} \in \mathbb{R}^{5N}$ is ordered accordingly. It represents the discretization of the flux integral in (2). Finally, \tilde{V} is a diagonal scaling matrix

$$\tilde{V} = \text{diag}(V, \dots, V) \in \mathbb{R}^{5N \times 5N} \quad (7)$$

with $V = \text{diag}(V_1, \dots, V_N) \in \mathbb{R}^{N \times N}$ where V_i is the volume of the control volume Ω_i .

In this work steady-state solutions are considered which are unchanging in time. That is, the steady-state $\mathbf{w}(t = \infty; \alpha)$ satisfies

$$\mathbf{0} = -\tilde{V}^{-1} \mathbf{R}(\mathbf{w}(t = \infty; \alpha)). \quad (8)$$

The angle of attack α is the most relevant parameter to this system; the steady-state described by (8) depends on the choice of α (not t).

3 Proper Orthogonal Decomposition for discretized flow solutions

Proper Orthogonal Decomposition (POD) is a method for obtaining the orthogonal basis Φ used in (1) in order to reduce a full order model to a reduced order one which can be solved in less computational time. The focus is on the application to discretized flow solutions. Refer to [20] for more information on the derivation of POD or [21] on the method of snapshots.

POD constructs Φ as follows. Assume that steady flow solutions $\mathbf{w}_i = \mathbf{w}(t = \infty; \alpha_i)$ solving (8) for different angles of attack α_i with $i = 1, \dots, M$ are given. These solutions \mathbf{w}_i are referred to as snapshots. The corresponding centered snapshot matrix is defined as

$$W = ((\mathbf{w}_1 - \bar{\mathbf{w}}) \dots (\mathbf{w}_M - \bar{\mathbf{w}})) \in \mathbb{R}^{5N \times M},$$

where $\bar{\mathbf{w}}$ is the average of the snapshots, i.e. $\bar{\mathbf{w}} = \frac{1}{M} \sum_{i=1}^M \mathbf{w}_i$. Defining the snapshot matrix centered around the average has the advantage that not the dynamics itself, but only the deviation from the average has to be modeled.

The orthogonal POD basis vectors are obtained by the singular value decomposition (SVD) of the scaled centered snapshot matrix $\tilde{V}^{\frac{1}{2}}W$. In fact, the left singular vectors are the desired vectors. Our approach follows the method of snapshots [21]: First the eigenvalue decomposition of $W^T \tilde{V} W \in \mathbb{R}^{M \times M}$ is computed

$$W^T \tilde{V} W = \Psi \Lambda \Psi, \quad (9)$$

where $\Lambda = \text{diag}(\lambda_1 \dots \lambda_M) \in \mathbb{R}^{M \times M}$ is a diagonal matrix, whose diagonal entries are the eigenvalues λ_i of $W^T \tilde{V} W$. Note that $\Psi \in \mathbb{R}^{M \times M}$ is the matrix of eigenvectors. It is orthogonal, since $W^T \tilde{V} W$ is symmetric.

The left singular vectors are then obtained via

$$\varphi_i = \frac{1}{\sqrt{\lambda_i}} W \psi_i.$$

They are orthogonal with respect to the L_2 scalar product

$$(\mathbf{w}_1, \mathbf{w}_2)_{\tilde{V}} = \mathbf{w}_1^T \tilde{V} \mathbf{w}_2 \quad (10)$$

with \tilde{V} as in (7), where $\mathbf{w}_1, \mathbf{w}_2$ of the form (6). These vectors constitute the so-called POD basis and are also referred to as modes.

After a possible truncation to $m \leq M$ modes, the basis can be written as a matrix

$$\Phi = (\varphi_1 \dots \varphi_m). \quad (11)$$

Note that the POD basis does not describe the dynamics itself, but the deviation from the mean $\bar{\mathbf{w}}$, since it has been subtracted from the snapshots. For this reason, a vector of the form $\Phi \mathbf{a}$ with suitable coefficients $\mathbf{a}^T = (a_1 \dots a_m) \in \mathbb{R}^m$ has to be shifted back by the average $\bar{\mathbf{w}}$ in order to approximate a flow, that is

$$\mathbf{w} = \Phi \mathbf{a} + \bar{\mathbf{w}}. \quad (12)$$

Note that since in each column of the snapshot matrix the mean $\bar{\mathbf{w}}$ is subtracted from a snapshot, the columns become linearly dependent. This can easily be verified by the fact that the sum of the columns is zero. Therefore the rank of the centered snapshot matrix is less than the number of columns, that is, $\text{rank}(W) \leq M - 1$. As a consequence the smallest eigenvalue in (9) is exactly zero and for this reason the corresponding M th mode should always be disregarded, since it carries no information whatsoever about the snapshots.

4 Missing Point Estimation

Missing Point Estimation (MPE) is a model order reduction technique which aims at reducing the computational costs for solving nonlinear reduced order systems. This is achieved by setting up the reduced order system such that it uses a suitable projection which avoids the costly evaluation of the right hand side of the original model for all components, see, e.g., (1) for the case of POD. Instead only a few components are selected, at which the right hand side is evaluated.

In the following a brief overview of MPE with emphasis on aerodynamic applications is given. For a more detailed and a more general account of MPE the reader is referred to [5].

Consider the spatially discretized governing equations (5). Replace $\mathbf{w}(t; \alpha)$ by the POD representation (12)

$$\frac{d\Phi\mathbf{a}(t; \alpha)}{dt} = -\tilde{V}^{-1}\mathbf{R}(\Phi\mathbf{a}(t; \alpha) + \bar{\mathbf{w}}) + \boldsymbol{\epsilon}_0. \quad (13)$$

This introduces the error $\boldsymbol{\epsilon}_0$. Note that $\frac{d\bar{\mathbf{w}}}{dt} = 0$, since the average is time-independent. Moreover, in (13) the entire $5N$ dimensional function \mathbf{R} has to be evaluated, even though the left hand side of the system is of dimension m .

The idea of MPE is to set up the reduced order model in such a way that the residual \mathbf{R} is to be evaluated only at a small subset of all the grid points. Let the indices of the points of this set be $\mathbb{X} = \{j_1, \dots, j_n\} \subset \{1, \dots, N\}$, where N is the total number of grid points, n is the number of the selected points and j_1, \dots, j_n their indices. By defining the filtering matrix for one flow variable as

$$P = (\mathbf{e}_{j_1} \quad \dots \quad \mathbf{e}_{j_n}) \in \mathbb{R}^{N \times n}, \quad (14)$$

with the j th unit vector $\mathbf{e}_j \in \mathbb{R}^N$ and the filtering matrix for all flow variables as $\tilde{P} = \text{diag}(P, \dots, P) \in \mathbb{R}^{5N \times 5n}$, a projection onto the chosen points $\mathbb{X} = \{j_1, \dots, j_n\}$ is given by $\Pi_{\tilde{P}} = \tilde{P}\tilde{P}^T$. Applying this projection to equation (13) yields

$$\tilde{P}\tilde{P}^T\Phi\frac{d\mathbf{a}(t; \alpha)}{dt} = -\tilde{P}\tilde{P}^T\tilde{V}^{-1}\mathbf{R}(\Phi\mathbf{a}(t; \alpha) + \bar{\mathbf{w}}) + \tilde{P}\tilde{P}^T\boldsymbol{\epsilon}_0.$$

As a next step orthogonality conditions are imposed upon the system, which state that $\tilde{P}\tilde{P}^T\Phi\frac{d\mathbf{a}(t; \alpha)}{dt} + \tilde{P}\tilde{P}^T\tilde{V}^{-1}\mathbf{R}(\Phi\mathbf{a}(t; \alpha) + \bar{\mathbf{w}})$ is orthogonal to the POD basis with respect to the L_2 scalar product (10),

$$\left(\varphi_j, \tilde{P}\tilde{P}^T \left[\Phi\frac{d\mathbf{a}(t; \alpha)}{dt} + \tilde{V}^{-1}\mathbf{R}(\Phi\mathbf{a}(t; \alpha) + \bar{\mathbf{w}}) \right] \right)_{\tilde{V}} = 0 \quad (15)$$

for $j = 1, \dots, m$. That is,

$$\Phi^T\tilde{V}\tilde{P}\tilde{P}^T \left[\Phi\frac{d\mathbf{a}(t; \alpha)}{dt} + \tilde{V}^{-1}\mathbf{R}(\Phi\mathbf{a}(t; \alpha) + \bar{\mathbf{w}}) \right] = 0. \quad (16)$$

This is equivalent to $\Phi^T\tilde{V}\tilde{P}\tilde{P}^T\boldsymbol{\epsilon}_0 = 0$, but this does not mean that the error $\boldsymbol{\epsilon}_0$ is not in the span of the POD basis. Rather, only the scaled projection of the error $\tilde{V}\tilde{P}\tilde{P}^T\boldsymbol{\epsilon}_0 \notin \text{spancol}(\Phi)$. For this reason the points of $\mathbb{X} = \{j_1, \dots, j_n\}$ have to be chosen with care. Moreover, the points have to be chosen such that the inverse $(\Phi^T\tilde{V}\tilde{P}\tilde{P}^T\Phi)^{-1}$ exists. See Section 4.2 for more details.

Premultiplying equation (16) formally with the inverse $(\Phi^T\tilde{V}\tilde{P}\tilde{P}^T\Phi)^{-1}$ yields the reduced MPE system

$$\frac{\partial\mathbf{a}}{\partial t} = -(\Phi^T\tilde{V}\tilde{P}\tilde{P}^T\Phi)^{-1}\Phi^T\tilde{P}\tilde{P}^T\mathbf{R}(\Phi\mathbf{a}(t; \alpha) + \bar{\mathbf{w}}). \quad (17)$$

Here $\tilde{V}\tilde{P}\tilde{P}^T\tilde{V}^{-1} = \tilde{P}\tilde{P}^T$ is used. Since the matrices $\tilde{P}\tilde{P}^T$ and \tilde{V} are diagonal, their multiplication is commutative.

For steady-state problems as considered in this work, the goal is to find solutions, for which

$$\mathbf{0} = -(\Phi^T \tilde{V} \tilde{P} \tilde{P}^T \Phi)^{-1} \Phi^T \tilde{P} \tilde{P}^T \mathbf{R}(\Phi \mathbf{a}(t; \alpha) + \bar{\mathbf{w}}) \quad (18)$$

holds which is equivalent to

$$\mathbf{0} = \Phi^T \tilde{P} \tilde{P}^T \mathbf{R}(\Phi \mathbf{a}(t; \alpha) + \bar{\mathbf{w}}).$$

The POD coefficients $\mathbf{a}(t; \alpha)$ obtained from solving the above system (18) are inserted into the affine POD representation (12) to obtain the reduced order solution.

Note that the reduced order system (17) is of the order $m \ll 5N$ and is thus of small complexity. Furthermore, due to the filtering of the residual, $\tilde{P}^T \mathbf{R}(\Phi \mathbf{a}(t; \alpha) + \bar{\mathbf{w}})$, only a few selected entries of the right hand side have to be evaluated which will accelerate the computation significantly.

Note that in the reduced system (17) the MPE projection is implicitly defined by

$$\Pi = \Phi(\Phi^T \tilde{V} \tilde{P} \tilde{P}^T \Phi)^{-1} \Phi^T \tilde{V} \tilde{P} \tilde{P}^T. \quad (19)$$

The projection of MPE catenates two different projections: one, which projects onto the selected points, and another one, which projects onto the POD subspace.

For this reason the MPE reduced order model is a projection method as described in [22, Chapter 5]: A solution to equation (13) is sought, which lies in a search subspace [22, Chapter 5]. In our case this search subspace is the affine POD subspace $\text{spancol}(\Phi)$. By imposing orthogonality conditions onto the equations as in (15) and (16) an approximation to (13) can be computed. The orthogonality conditions define a subspace of constraints [22, Chapter 5], which is given by $\text{spancol}(\tilde{P} \tilde{P}^T \tilde{V} \Phi)$. Note that the constraint subspace is dependent on the POD subspace, but is restricted to the point selection. Since the two subspaces - the search and the constraint subspace - are in general not identical, Π is a Petrov-Galerkin projection [23, p. 279] and Π is in general not orthogonal, but oblique.

4.1 Solving the reduced order model

In order to solve the reduced order model (17), consider an implicit Euler scheme. This yields

$$\frac{\Delta \mathbf{a}}{\Delta t} = -\mathbf{r}(\mathbf{a}(t + \Delta t; \alpha)),$$

where $\Delta \mathbf{a} = \mathbf{a}(t + \Delta t; \alpha) - \mathbf{a}(t; \alpha)$, Δt is the time step size and

$$\mathbf{r}(\mathbf{a}(t; \alpha)) = (\Phi^T \tilde{V} \tilde{P} \tilde{P}^T \Phi)^{-1} \Phi^T \tilde{P} \tilde{P}^T \mathbf{R}(\Phi \mathbf{a}(t; \alpha) + \bar{\mathbf{w}}) \in \mathbb{R}^m.$$

By inserting the Taylor expansion $\mathbf{r}(\mathbf{a}(t + \Delta t; \alpha)) \approx \mathbf{r}(\mathbf{a}(t; \alpha)) + \frac{\partial \mathbf{r}}{\partial \mathbf{a}} \Delta \mathbf{a}$ into the above equation,

$$\left(\frac{1}{\Delta t} + \frac{\partial \mathbf{r}}{\partial \mathbf{a}} \right) \Delta \mathbf{a} = \mathbf{r}(\mathbf{a}(t; \alpha)) \quad (20)$$

is obtained. As we are searching for the steady state, $\Delta t \rightarrow \infty$ can be set. This yields the Newton method, which finds the root in (18).

In our implementation we use a more refined algorithm to find the root of (18) which is called Powell's Dog Leg method [24]. It combines the Newton method with the steepest descent direction. While the steepest descent method offers good performance in the beginning, the Newton method converges quickly in the final stages [25]. We use an implementation of Powell's Dog Leg method realized in the function *fsolve* of the subpackage *optimize* of *scipy* [26], which is a wrapper around MINPACK *hybrd* and *hybrj* algorithms [27]. As an initial condition for the root finding algorithm, the mean flow is chosen, i.e. the corresponding POD coefficients are $\mathbf{a} = \mathbf{0}$.

4.2 Point Selection

Obviously, the choice of \tilde{P} plays a significant role in the performance of the MPE. It has an influence both on the accuracy of the solution and the time efficiency of the computation.

While in other publications [5, 6, 8, 9] the points are chosen based on minimizing the condition number of the matrix¹ $M = \Phi^T \tilde{P} \tilde{P}^T \Phi$ or minimizing the alias error $\|\Phi^T \tilde{P} \tilde{P}^T \Phi - I\|$, this is too time-consuming even for the application to two-dimensional, steady aerodynamic problems with grids of the order of tens of thousands. For this reason we choose the points based on the flow physics only.

In particular, since the angle of attack is the only varying parameter to the system in this work, the farfield points play an important role. This is due to the fact that the farfield points have to satisfy the freestream boundary conditions for the given angle of attack. For this reason there is a strong dependence of the farfield on the parameter.

While for CFD computations the information on the farfield has to be transported to the airfoil by advancing in (pseudo-)time, in the reduced order model there is a coupling between the farfield points and the points in the region close to the surface via the POD basis. Hence, when the flow variables on the farfield points are close to those of the real solution, then it is expected that the same holds true for the region around the surface of the airfoil for elliptic problems. In the elliptic case any point in the flow field influences the entire field. Consequently, a change in a boundary point also effects all other points in the computational domain. Steady, subsonic flows - which are considered in this work - are (mainly) elliptic in nature (see [11, Chapter 1] and [28, p.17]).

Besides the farfield points, it might be desirable to include the points lying in and close to the boundary layer. Specifics for the test cases will be given in Section 5.

Remark 1 *Note that the number of points n has to be such that $5n \geq m$. This is due to the fact that otherwise the matrix $\Phi^T \tilde{V} \tilde{P} \tilde{P}^T \Phi$ in the projection matrix Π of the MPE is singular. In any case, it has to be verified that $\Phi^T \tilde{V} \tilde{P} \tilde{P}^T \Phi$ in the projection matrix Π is nonsingular for the particular choice of \tilde{P} .*

4.3 Error estimation

In this subsection an error estimate for the reduced order MPE system shall be derived for equations of the form $\frac{d\mathbf{w}(t)}{dt} = \mathbf{f}(\mathbf{w}(t))$. It is intentionally not formulated for the governing equations of CFD, since it is assumed that the right hand side \mathbf{f} is Lipschitz continuous. This assumption is not valid for the governing equations of CFD, if flows with shocks are considered. The error estimator will, however, give a theoretical insight into the error of MPE reduced order system.

Note that the error estimate is very similar to the one given in [18], since both methods, MPE and the DEIM, are nonlinear model order reduction techniques, which use projections to obtain an efficiently evaluable right hand side for the reduced model.

As in [18], the least upper bound *logarithmic Lipschitz constants* with respect to an inner product (\cdot, \cdot) is used. It is defined for a map $\mathbf{f} : \mathcal{W} \subset \mathbb{R}^N \rightarrow \mathbb{R}^N$ as

$$M[\mathbf{f}] := \sup_{\mathbf{u} \neq \mathbf{v}} \frac{(\mathbf{u} - \mathbf{v}, \mathbf{f}(\mathbf{u}) - \mathbf{f}(\mathbf{v}))}{\|\mathbf{u} - \mathbf{v}\|^2}. \quad (21)$$

This definition can be found in [29].

Theorem 1 *Let the error of the solution of the reduced order MPE system be given by $\epsilon(t) = \mathbf{w}(t) - \hat{\mathbf{w}}(t)$, where $\mathbf{w}(t)$ is the full order and $\hat{\mathbf{w}}(t)$ the reduced order model solution for $t \in [0, T]$. That is, $\mathbf{w}(t)$ solves the system $\frac{d\mathbf{w}(t)}{dt} = \mathbf{f}(\mathbf{w}(t))$ with the initial condition $\mathbf{w}(0) = \mathbf{w}_0$ and $\hat{\mathbf{w}}(t)$ solves $\frac{d\hat{\mathbf{w}}(t)}{dt} = \Pi \mathbf{f}(\hat{\mathbf{w}}(t))$ with $\hat{\mathbf{w}}(0) = \Phi \Phi^T \mathbf{w}_0$. Here Π is defined as in (19) and Φ is the truncated POD basis (11). Furthermore, let the right hand side of the full order system \mathbf{f} be Lipschitz*

¹Note that the scaling with the volume matrix \tilde{V} is not included in the matrix, since in [5, 6] the Euclidean scalar product instead of the L_2 scalar product is used.

continuous with the Lipschitz constant $L_{\mathbf{f}}$ and let $M[\Pi\mathbf{f}]$ be the logarithmic Lipschitz constant of $\Pi\mathbf{f}$ as in (21). Then the error $\boldsymbol{\epsilon}(t)$ can be estimated by

$$\int_0^T \|\boldsymbol{\epsilon}(t)\|^2 dt \leq C \left(\int_0^T \|\mathbf{w}(t) - \Phi\Phi^T \mathbf{w}(t)\|^2 dt + \int_0^T \|\mathbf{f}(\mathbf{w}(t)) - \Phi\Phi^T \mathbf{f}(\mathbf{w}(t))\|^2 dt \right),$$

with

$$\begin{aligned} C &:= \max\{1 + 2c_M\beta^2, 2c_M\gamma^2\}, \\ \beta &= L_{\mathbf{f}}\|\Phi^T\Pi\|, \quad \gamma = \|\Phi^T\Pi\bar{\Phi}\|, \\ c_M &= \begin{cases} \frac{1}{M[\Pi\mathbf{f}]}(e^{2M[\Pi\mathbf{f}]T} - 1), & M[\Pi\mathbf{f}] \neq 0, \\ 2T, & M[\Pi\mathbf{f}] = 0, \end{cases} \end{aligned}$$

where $\bar{\Phi}$ is the orthogonal complement of the truncated POD basis, i.e. $\bar{\Phi} \oplus \Phi = \mathbb{R}^{5N}$.

The proof is given in [10].

Note that Theorem 1 states that the error of the MPE reduced system can be bounded from above by a multiple of the sum of the projection error with respect to the POD subspace of the solutions $\mathbf{w}(t)$ and the projection error in the POD subspace of the right hand side $\mathbf{f}(t)$ of the system. If all points are considered in the MPE, that is $\Pi = \Phi\Phi^T$, it directly follows that $\gamma = \|\Phi^T\Pi\bar{\Phi}\| = 0$. Thus, the projection error of the right hand side $\mathbf{f}(t)$ can be neglected in the error estimation in case of Galerkin projection.

5 Numerical Experiments

In this section MPE is applied to high-lift two-element airfoils, on the one hand in a setting as during take-off, on the other hand during landing. The flows considered in both test cases are in the subsonic flow regime. They will be modeled by the RANS equations (2) to accurately capture the flow physics. The underlying geometry is known as the DLR-F15 configuration [30]. It is a configuration of industrial relevance.

For all computations (except the snapshot computations) an AMD Athlon™ 64 X2 Dual Core Processor 4400+ with 2 GB RAM is used. The computer is operated under Debian GNU/LINUX.

5.1 High-lift take-off configuration

As a first test case the viscous flow past a section cut of the DLR-F15 slotted wing-flap configuration at a freestream Mach number of $M_\infty = 0.22$, a Reynolds number of 10.549 million and a reference temperature of 118 K is considered. Given a set of M snapshots, that is, steady-state solutions for a certain fixed Mach number and M different angles of attack $\mathcal{A} = \{\alpha_1, \alpha_2, \dots, \alpha_M\}$, our goal is to predict the flow solution at $\alpha \notin \mathcal{A}$ at the same fixed Mach number with the help of MPE. In particular, for this test case $M = 5$ and $\mathcal{A} = \{0^\circ, 2^\circ, 4^\circ, 6^\circ, 8^\circ\}$ has been chosen, as this covers a range of angles of attack without flow separation. The solution will be predicted at $\alpha = 7^\circ$. With the flow solution the lift and drag coefficient of the airfoil can be determined.

The snapshots are computed with the flow solver TAU [31, 32] by solving the Navier-Stokes equation using the Spalart-Allmaras one-equation turbulence model [19, Subsection 7.2.1]. The computation of the first snapshot at the lowest angle of attack ($\alpha = 0^\circ$) is initialized with freestream conditions, while the others are computed using the snapshot with the nearest angle of attack (two degrees below the current α) as a start solution. This procedure is followed to avoid aerodynamic hysteresis problems, where more than one solution may exist at the same angle of attack.

Convergence to steady-state is detected in the snapshot computations based on the absolute change in the aerodynamic coefficients. More precisely, if the change in the aerodynamic coefficients is below a user-defined tolerance over 100 successive iterations, then the solution is considered to be converged. The tolerances for the change in the lift c_l , drag c_d and pitching moment c_m coefficient are set to 10^{-3} , 10^{-5} , and 0.1, respectively.

All computations are carried out on a hybrid grid, which is structured near the surface of the configuration and unstructured otherwise. It consists of 50,809 grid points (control volumes) and is depicted in Figure 1. Hence, the number of unknowns to be determined is $5 \cdot 50,809 = 254,045$.

Influence of the number of modes used (Choice of m) First the POD basis is computed. The relative information content contained in each mode in the L_2 sense is given by

$$E(j) = \frac{\lambda_j}{\sum_{i=1}^M \lambda_i}, \quad (22)$$

where λ_i are the eigenvalues as in (9) [33]. It is given in Table 1. The relative information content of the last mode has to be exactly zero as stated in Section 3. Furthermore, note that the first mode contains more than 99.9 % of the information. This is partially due to the L_2 scalar product as explained in [34].

Next we investigate the impact of using an increasing number of modes in the MPE model to simulate the solution at an angle of attack of $\alpha = 7^\circ$, that is, (18) is solved for $\alpha = 7^\circ$ varying the number of modes used. The filtering matrix \tilde{P} is set up using all farfield points.

j	1	2	3	4	5
$E(j)$	$9.99571 \cdot 10^{-1}$	$4.27176 \cdot 10^{-4}$	$1.30249 \cdot 10^{-6}$	$1.08424 \cdot 10^{-7}$	0

Table 1: Relative information content of the modes.

Table 2 shows the aerodynamic coefficients as well as the associated relative errors with respect to the CFD reference solution for the different truncation levels. That is, e.g. the error for the lift coefficient is given by $(c_l^{MPE} - c_l^{CFD})/c_l^{CFD} \cdot 100$.

# of modes	# of iters	c_l	error	c_d	error
$m = 1$	4	2.698	0.48%	$5.035 \cdot 10^{-2}$	3.90%
$m = 2$	4	2.699	0.52%	$4.891 \cdot 10^{-2}$	0.93%
$m = 3$	5	2.699	0.52%	$4.891 \cdot 10^{-2}$	0.93%
$m = 4$	6	2.696	0.41%	$4.865 \cdot 10^{-2}$	0.39%
CFD	1415	2.685		$4.846 \cdot 10^{-2}$	

Table 2: Lift and drag coefficients predicted at $\alpha = 7^\circ$ for different numbers of modes.

The error in the drag coefficient c_d decreases with the number of modes. However, there is only a slight improvement when using more than two modes. The error of the lift coefficient c_l is almost constant and is smallest, when all modes are considered.

In addition, Table 2 reveals the number of iterations (# of iters) to solve equation (20). For MPE the number of iterations increases, the more modes are taken into account.

Since the prediction of the aerodynamic coefficient is best when choosing all modes, we will consider all of them from now on. Hence from here on, the reduced order MPE system is a system of dimension 4×4 while the original CFD system is of dimension $254,045 \times 254,045$. Bearing in mind that the filtering matrix employed in MPE determines at how many grid points \mathbf{R} is evaluated, while for CFD the entire $\mathbf{R} \in \mathbb{R}^{254,045}$ has to be evaluated, it is obvious that MPE is much faster than a full CFD computation.

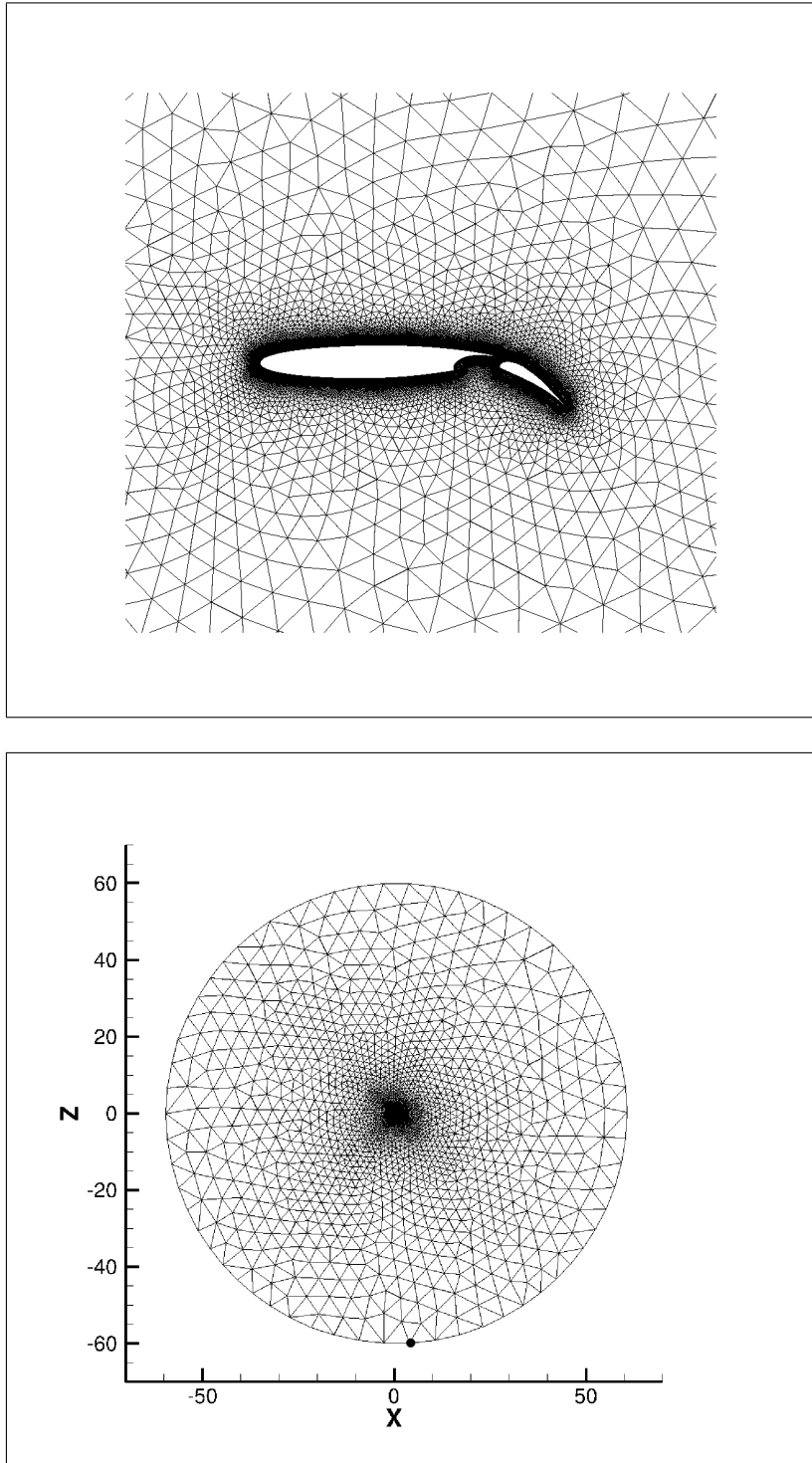


Figure 1: The hybrid grid of the wing-flap configuration under take-off conditions with $N = 50,809$ points.

Influence of the filtering matrix (Choice of P and n) The next question considered is which impact the choice of filtering matrix has on the quality of the MPE solution. Recall, that the filtering matrix not only determines at how many grid points \mathbf{R} has to be evaluated, but also at which ones. Five different point selections are considered:

Due to the fact that the values of the farfield points are closely connected to the angle of attack, it is inevitably to make use of them. Point selection I uses only the single farfield point that is marked in the bottom plot in Figure 1. At $\alpha = 0^\circ$ the onflow in this point is parallel to the tangent of the computational domain. When the angle of attack is increased, the flow will enter the control volume more and more directly. Therefore, the angle of attack has significant influence on the point.

Point selection II uses all 60 farfield points.

In point selection III the farfield points are complemented by points from a part of the boundary layer. The points having a distance between 0 and $5.0 \cdot 10^{-5}$ grid units from the surface of the airfoil² are chosen. This region is part of the boundary layer. Thus point selection III gives an insight of the influence the boundary layer has on the solution of the MPE. In this setting a total of 12,940 points is considered.

In point selection IV the farfield points are complemented by points which are right outside of the boundary layer. For this particular test case the points chosen have a distance between 0.02 and 0.5 units from the surface of the airfoil. In this way 6,252 points are used in the MPE.

Finally, along with the farfield points we choose another set of points, which is a bit further away from the boundary, but still close to the surface. All points having a distance between 0.1 and 1.0 units from the surface are chosen.

A summary of the different point selection settings is given by Table 3.

point selection	# of points	min dist	max dist
I (1 farfield point)	1	-	-
II (entire farfield (FF))	60	99.0	101.0
III (FF + some BL points)	12940	0.0	$5.0 \cdot 10^{-5}$
IV (FF + points close to BL)	6252	0.02	0.5
V (FF + pts further from BL)	1273	0.1	1.0

Table 3: Definition of the point selections, where min/max dist stands for the minimal and maximal distance from the surface of the configuration in grid units (length of the airfoil = 0.6 grid units). FF and BL stands for the farfield and the boundary layer, resp.

Table 4 shows the lift and drag coefficients as well as the corresponding errors for the different point selections. It can be seen that the error is smallest for point selection scenarios IV and V, for which - additionally to the farfield - points outside of the boundary layer are chosen.

point selection	# of iters	c_l^{MPE}	error	c_d^{MPE}	error
I	22	2.696	0.41%	$4.864 \cdot 10^{-2}$	0.37%
II	6	2.696	0.41%	$4.865 \cdot 10^{-2}$	0.39%
III	11	2.708	0.86%	$4.967 \cdot 10^{-2}$	2.5%
IV	6	2.688	0.11%	$4.798 \cdot 10^{-2}$	0.99%
V	6	2.693	0.30%	$4.842 \cdot 10^{-2}$	0.08%

Table 4: Lift and drag coefficients.

In fact, scenario IV is best for the lift and V for the drag coefficient. The worst result is obtained when the boundary layer is included. This indicates that the turbulent region lacks

²Note that the airfoil has a reference length of 0.6 grid units.

spatial correlation with the rest of the flowfield. Matching the flow physics in the POD subspace for this region amounts to overfitting noisy, uncorrelated data.

Based on the number of iterations, scenarios I and III are the most ineffective point selections. However, it has to be emphasized that in each iteration the residual evaluation of scenario I is very efficient, since it has to be evaluated for a single point only.

Note that when taking into account only the farfield points, a good result with an error less than one percent is achieved. Due to the fact that these points can also be easily identified, this seems to be a practical approach to finding a point selection.

Next the quality of the pressure distribution c_p of the MPE solution is investigated, where the residuals are evaluated at all farfield points. In Figure 2 both the reference c_p computed with CFD and that of the MPE using all four modes and with point selection II is shown. Obviously, they match very well and there is only a slight deviation at the stagnation point.

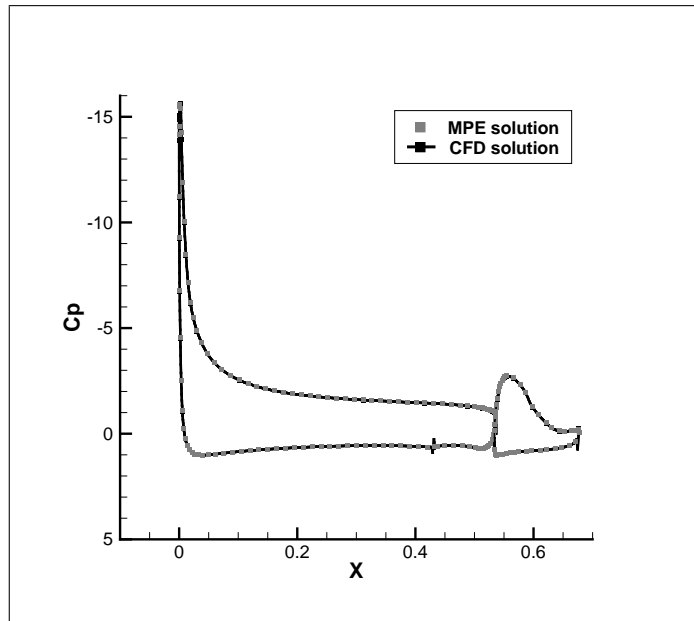


Figure 2: Pressure distribution on the surface of the take-off configuration.

Solutions at some intermediate angles of attack In order to demonstrate that the MPE model can be used for predicting solutions at other intermediate angles of attack (AoA) (18) has also been solved for $\alpha \in \{1^\circ, 3^\circ, 5^\circ\}$, using the same POD basis as in the rest of this section and the filtering matrix using all farfield points. Table 5 shows the aerodynamic coefficients and their errors in comparison to the corresponding CFD solution. Note that all relative errors are less than one percent.

AoA	c_l^{MPE}	error	c_d^{MPE}	error
1°	2.112	0.61%	$3.465 \cdot 10^{-2}$	0.84%
3°	2.310	0.26%	$3.828 \cdot 10^{-2}$	0.36%
5°	2.495	0.12%	$4.234 \cdot 10^{-2}$	0.37%
7°	2.696	0.41%	$4.865 \cdot 10^{-2}$	0.39%

Table 5: Lift and drag coefficients at different angles of attack.

Figure 3 shows the plots of the lift and drag coefficient over the angle of attack. It can be seen that the MPE solutions given by the asterisks closely match the CFD reference solution.

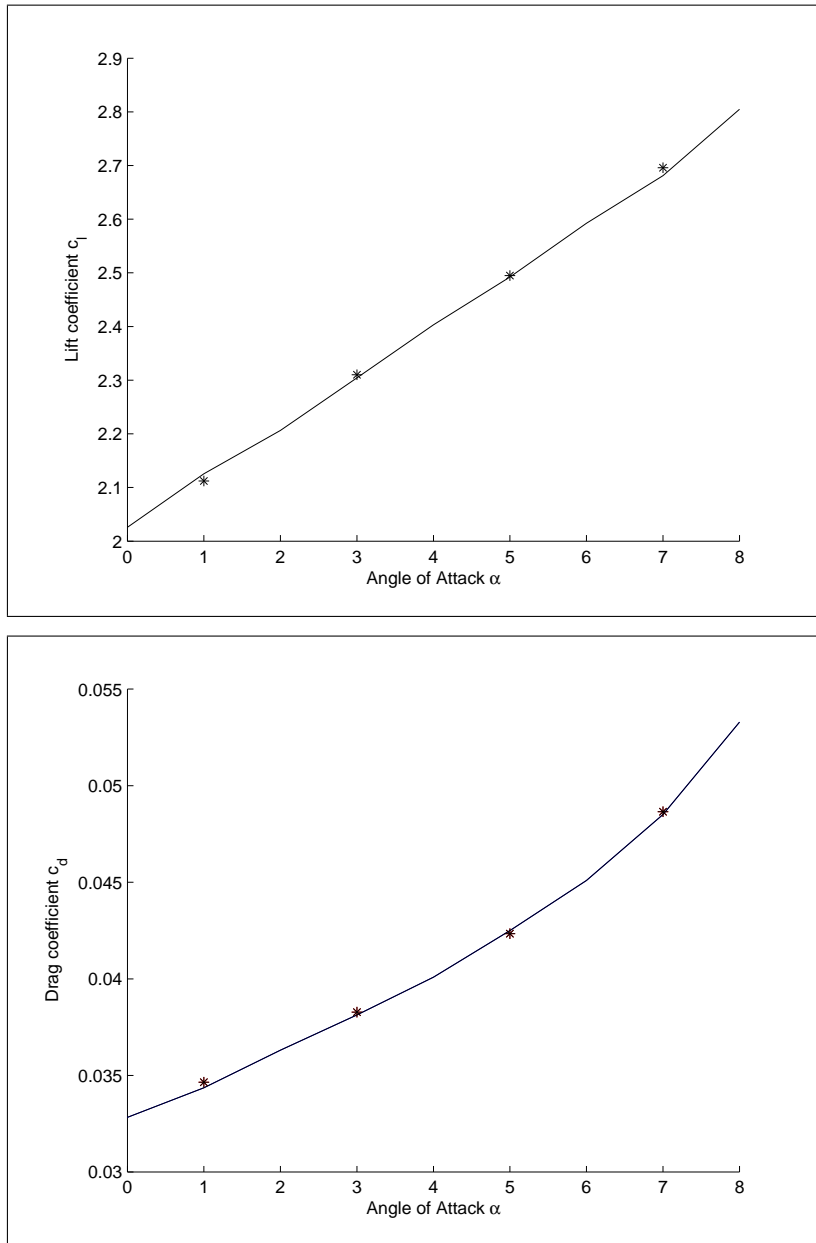


Figure 3: Aerodynamic coefficients plotted over the angle of attack. The line represents the coefficients of the CFD reference solution and the asterisks those of the MPE solution.

Comparison with Thin Plate Spline (TPS) interpolation Finally, the performance of MPE is compared to interpolating the snapshots as introduced in [35].

In order to be able to interpolate the snapshots, they are first projected onto the POD subspace. That is,

$$a_i(\alpha_j) = (\varphi_i, \mathbf{w}_j)_{L_2}, \quad i = 1, \dots, d, \quad j = 1, \dots, m,$$

which yields the POD coefficients of the snapshots $\mathbf{w}_1, \dots, \mathbf{w}_m$.

These POD coefficients are then interpolated to get a set of coefficients $a_i(\alpha^*)$ for the desired angle of attack α^* . In this work the interpolation method Thin Plate Spline (TPS) interpolation is employed [36].

Table 6 reveals the aerodynamic coefficients as well as their relative errors for the just described interpolation methodology. For $\alpha = 1^\circ$ and $\alpha = 7^\circ$ MPE performs significantly better than TPS interpolation, for the other two angles TPS interpolation performs slightly better than MPE. For the angles $\alpha = 1^\circ$ and $\alpha = 7^\circ$ there is only one neighboring snapshot with a lower or higher angle of attack. This poses a problem for TPS interpolation and reveals a deficiency of the interpolation approach to yield good solutions in a global sense. In this sense, MPE outperforms TPS interpolation.

AoA	c_l^{TPS}	error	c_d^{TPS}	error
1°	2.115	0.47%	$3.334 \cdot 10^{-2}$	2.97%
3°	2.304	0.00%	$3.807 \cdot 10^{-2}$	0.18%
5°	2.497	0.20%	$4.245 \cdot 10^{-2}$	0.12%
7°	2.697	0.45%	$4.754 \cdot 10^{-2}$	1.90%

Table 6: Lift and drag coefficients obtained with TPS interpolation.

5.2 High-lift landing configuration

As a second test case a section cut of the DLR-F15 high-lift wing-flap configuration under landing conditions is considered. The viscous flow around this configuration modeled by the Navier-Stokes equations is considered at an atmospheric pressure of 101325 Pa, a temperature of 15°C (288.15K) and a speed of $|\mathbf{v}_\infty| = 53$ m/s, which corresponds to a Mach number of $M_\infty = 0.1558$. This setting correlates to a Reynolds number of 2.177 million.

This second test case is considered to demonstrate that the MPE works on a different grid (see Figure 4). Furthermore it involves slightly different flow physics compared to the previous test case.

Snapshots are computed for angles of attack of $\alpha \in \{0^\circ, 2^\circ, 4^\circ, 6^\circ, 8^\circ\}$ with the TAU [31, 32] code using the Spalart-Allmaras turbulence model as before. The grid is a hybrid one, structured in the region of the boundary layer and unstructured elsewhere. It is shown in Figure 4 and contains $N = 73,474$ mesh points. Hence, the number of unknowns to be determined is $5 \cdot 73,474 = 367,370$.

Influence of the number of used modes (Choice of m) Tables 7 and 8 provide the same information for the example considered here as Tables 1 and 2 for the previous test case. As before the first mode contains 99.9% of the information. In contrast to the previous example the error of the drag coefficient is less for two than for three modes, but it is smallest when all modes are considered. For this reason we will carry out all computations with all modes henceforth. Hence from here on, the reduced order MPE system is a system of dimension 4×4 while the original CFD system is of dimension $367,370 \times 367,370$. As for MPE in contrast to CFD not the entire \mathbf{R} has to be evaluated, it is obvious that MPE is much faster than a full CFD computation.

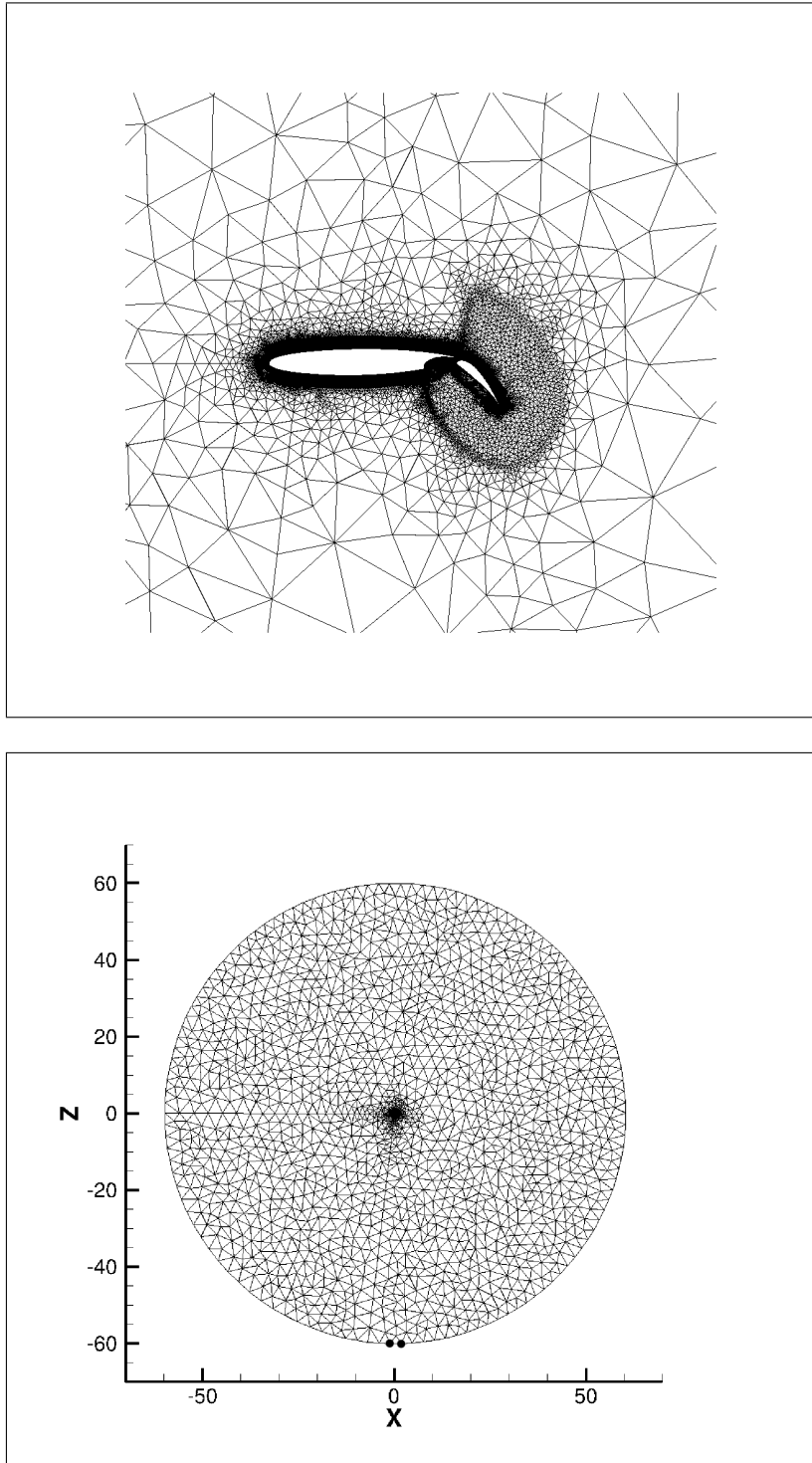


Figure 4: The hybrid grid of the DLR-F15 configuration under landing conditions with $N = 73,474$ points.

j	1	2	3	4	5
$E(j)$	$9.99579 \cdot 10^{-1}$	$4.209600 \cdot 10^{-4}$	$1.88304 \cdot 10^{-7}$	$9.33441 \cdot 10^{-8}$	0

Table 7: Relative energy content of the modes.

# of modes	# of iters	c_l	error	c_d	error
$m = 1$	3	2.539	0.27%	$8.307 \cdot 10^{-2}$	12.61%
$m = 2$	3	2.541	0.20%	$9.513 \cdot 10^{-2}$	0.07%
$m = 3$	4	2.542	0.16%	$9.519 \cdot 10^{-2}$	0.14%
$m = 4$	4	2.544	0.08%	$9.510 \cdot 10^{-2}$	0.04%
CFD	1346	2.546		$9.506 \cdot 10^{-2}$	

Table 8: Lift and drag coefficients predicted at $\alpha = 3^\circ$ for different numbers of modes.

Influence of the selected points (Choice of P and n) For investigating the influence of the point selection on the solution of the MPE, similar point selection settings as in the previous test case are used. However, they have to be adjusted to the computational grid since for example the boundary layer has a different thickness for this mesh. Therefore the minimal and maximal distance for the definition of the points for settings IV are different. Specifics are given in Table 9.

point selection	# of points	min distance	max distance
I (1 farfield point)	2	-	-
II (entire farfield (FF))	125	99.0	101.0
III (FF + some BL points)	10974	0.0	$5.0 \cdot 10^{-5}$
IV (FF + points close to BL)	2360	0.07	0.5
V (FF + pts further from BL)	1882	0.1	1.0

Table 9: Definition of the point selections, where min/max dist stands for the minimal and maximal distance from the surface of the configuration in grid units (length of the airfoil = 0.6 grid units). FF and BL stands for the farfield and the boundary layer, resp.

Note that point selection setting I is given by the points marked in the bottom plot in Figure 4. As before, this is chosen such that the onflow is parallel to the tangent of the computational domain.

Table 10 presents the aerodynamic coefficients for the different point selection settings. As in the previous test case setting I, which is given by two of the farfield points shown in Figure 4, gives good results. It needs the most iterations, but the residual \mathbf{R} is evaluated only at 2 points, so that the low number of function evaluations makes up for the high number of iterations.

For all other point selections, both the lift and drag coefficient are mostly the same. As before since the farfield points can easily be identified, this is the most effective strategy. In Figure 5 the pressure distribution on the surface of the MPE solution considering only the farfield points and of the CFD reference solution is visualized. Obviously, both match very closely.

Solutions at some intermediate angles of attack Table 11 gives an overview of predicted aerodynamic coefficients and their errors for some intermediate angles of attack, namely $\alpha \in \{1^\circ, 5^\circ, 7^\circ\}$. In fact, all relative errors are below 0.27%.

Figure 6 shows the lift and drag versus the angle of attack. As in the previous test case the lift and drag coefficient of the MPE solution (represented by the asterisks) match those of the reference solution (given by the line).

point selection	# of iters	c_l^{MPE}	error	c_d^{MPE}	error
I	10	2.541	0.20%	$9.533 \cdot 10^{-2}$	0.28%
II	4	2.544	0.08%	$9.510 \cdot 10^{-2}$	0.04%
III	4	2.544	0.08%	$9.511 \cdot 10^{-2}$	0.05%
IV	5	2.544	0.08%	$9.510 \cdot 10^{-2}$	0.04%
V	5	2.544	0.08%	$9.510 \cdot 10^{-2}$	0.04%
CFD	1346	2.546		$9.506 \cdot 10^{-2}$	

Table 10: Lift and drag coefficients.

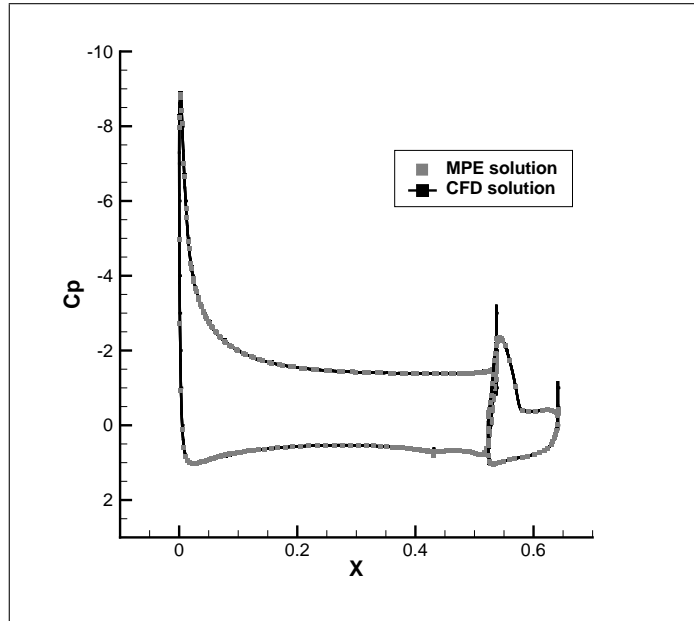


Figure 5: Pressure distribution on the surface of the landing configuration.

AoA	c_l^{MPE}	error	c_d^{MPE}	error
1°	2.329	0.09%	$9.075 \cdot 10^{-2}$	0.15%
3°	2.544	0.08%	$9.510 \cdot 10^{-2}$	0.04%
5°	2.747	0.18%	$1.003 \cdot 10^{-1}$	0.19%
7°	2.963	0.27%	$1.061 \cdot 10^{-1}$	0.19%

Table 11: Lift and drag coefficients for different angles of attack.

Comparison with Thin Plate Spline (TPS) interpolation Finally, the performance of MPE and TPS interpolation is compared. As can be seen from Table 12 in a global sense MPE outperforms TPS interpolation also for this test case.

6 Conclusions

A POD-based model order reduction method, called Missing Point Estimation (MPE), for efficiently computing steady subsonic flows has been discussed. The method remedies the POD-inherent problem of the dependence of the reduced order model on the degrees of freedom of the

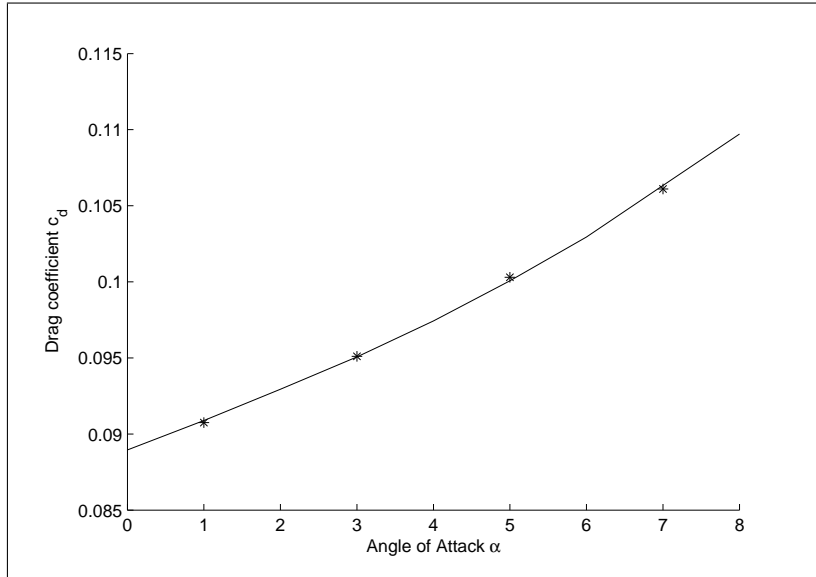
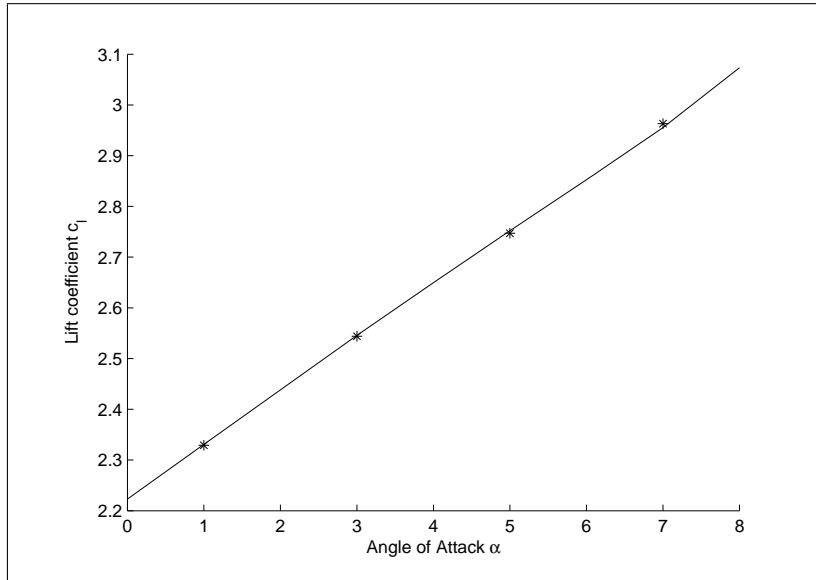


Figure 6: Aerodynamic coefficients plotted over the angle of attack. The line represents the coefficients of the CFD reference solution and the asterisks those of the MPE solution.

AoA	c_l^{TPS}	error	c_d^{TPS}	error
1°	2.330	0.04%	$8.941 \cdot 10^{-2}$	1.63%
3°	2.545	0.04%	$9.511 \cdot 10^{-2}$	0.05%
5°	2.751	0.04%	$1.002 \cdot 10^{-1}$	0.10%
7°	2.962	0.24%	$1.047 \cdot 10^{-1}$	1.51%

Table 12: Lift and drag coefficients obtained with TPS interpolation.

original problem. Error estimation in continuous ODE setting has been tackled.

The proposed method is tested for two different complex high-lift airfoils; one under take-off and the other under landing conditions. Given snapshots (steady flow solutions at different angles of attack) intermediate angles are computed with the MPE. For both airfoils it was demonstrated that considering only the farfield points for the filtering matrix suffices to get very accurate predictions of the aerodynamic coefficients as well as the pressure distribution on the surface at angles of attack not include in the snapshot basis. Since the farfield points can very easily be identified and are only very few compared to those in the rest of the flow field, the farfield seems to be a practical as well as efficient point selection. A large gain in computational efficiency is obtained. Finally, for the two test cases considered, MPE outperformed TPS interpolation in terms of accuracy in a global sense.

Acknowledgement

The research of the first author was supported by the German Federal Ministry of Economics and Technology (BMWi), grant no. 20 A 08 01 D.

The work of the German Aerospace Center (DLR) was supported in part by the European Regional Development Fund, Economic Development Fund of the Federal German State of Lower Saxony, contract/grant number: W3-80026826, and also by the German Federal Ministry of Economics and Technology (BMWi), grant no. 20 A 08 01 A.

References

- [1] C. Rowley, T. Colonius, R. Murray, Model reduction for compressible flows using POD and Galerkin projection, *Physica D: Nonlinear Phenomena* 189 (1-2) (2004) 115–129.
- [2] D. J. Lucia, P. I. King, P. S. Beran, Reduced order modeling of a two-dimensional flow with moving shocks, *Computers & Fluids* 32 (7) (2003) 917 – 938.
- [3] D. Lucia, P. Beran, W. Silva, Reduced-order modeling: new approaches for computational physics, *Progress in Aerospace Sciences* 40 (1-2) (2004) 51–117.
- [4] P. Astrid, Reduction of process simulation models: A proper orthogonal decomposition approach, Ph.D. thesis, Technische Universiteit Eindhoven (2004).
- [5] P. Astrid, S. Weiland, K. Willcox, T. Backx, Missing point estimation in models described by proper orthogonal decomposition, *IEEE Transactions on Automatic Control* 53 (10) (2008) 2237–2251.
- [6] P. Astrid, A. Verhoeven, Application of Least Squares MPE technique in the reduced order modeling of electrical circuits, in: *Proceedings of the 17th Int. Symp. MTNS, 2006*, pp. 1980–1986.

- [7] M. A. Cardoso, L. J. Durlofsky, P. Sarma, Development and application of reduced-order modeling procedures for subsurface flow simulation, *International Journal for Numerical Methods in Engineering* 77 (9) (2009) 1322–1350.
- [8] A. Vendl, H. Faßbender, Efficient POD-based Model Order Reduction for steady aerodynamic applications, in: C. Poloni, D. Quagliare, J. Périaux, N. Gauger, K. Giannakoglou (Eds.), *Evolutionary and deterministic methods for design, optimization and control, EUROGEN 2011*, CIRA, Capua, Italy, 2011, pp. 296–309.
- [9] A. Vendl, H. Faßbender, Missing point estimation for steady aerodynamic applications, *PAMM* 11 (1) (2011) 839–840.
- [10] A. Vendl, *Projection-based model order reduction for aerodynamic applications*, Ph.D. thesis, TU Braunschweig (2013).
- [11] K. A. Hoffmann, S. T. Chiang, *Computational Fluid Dynamics Volume I*, 4th Edition, Engineering Education System, Wichita, 2000.
- [12] M. A. Grepl, Y. Maday, N. C. Nguyen, A. T. Patera, Efficient reduced-basis treatment of nonaffine and nonlinear partial differential equations, *ESAIM-Mathematical Modelling and Numerical Analysis (M2AN)* 41 (3) (2007) 575–605.
- [13] N. C. Nguyen, J. Peraire, An efficient reduced-order modeling approach for non-linear parametrized partial differential equations, *International Journal for Numerical Methods in Engineering* 76 (2008) 27–55.
- [14] S. Chaturantabut, D. C. Sorensen, J. C. Steven, Nonlinear model reduction via discrete empirical interpolation, *SIAM Journal on Scientific Computing* 32 (5) (2010) 2737–2764.
- [15] D. Galbally, K. Fidkowski, K. Willcox, O. Ghattas, Non-linear model reduction for uncertainty quantification in large-scale inverse problems, *International Journal for Numerical Methods in Engineering* 81 (12) (2010) 1581–1608.
- [16] K. Carlberg, C. Farhat, C. Bou-Mosleh, Efficient non-linear model reduction via a least-squares Petrov–Galerkin projection and compressive tensor approximations, *International Journal for Numerical Methods in Engineering* 86 (2) (2011) 155–181.
- [17] D. Ryckelynck, A priori hyperreduction method: an adaptive approach, *Journal of Computational Physics* 202 (1) (2005) 346–366.
- [18] D. C. Sorensen, S. Chaturantabut, A State Space Error Estimate for POD-DEIM Nonlinear Model Reduction, *Siam Journal on Numerical Analysis* 50 (1) (2012) 46–63.
- [19] J. Blazek, *Computational Fluid Dynamics: Principles and Applications*, 1st Edition, Elsevier, 2001.
- [20] P. Holmes, J. L. Lumley, G. Berkooz, *Turbulence, Coherent Structures, Dynamical Systems and Symmetry*, Cambridge, New York, 1996.
- [21] L. Sirovich, Turbulence and the dynamics of coherent structures. Part I: Coherent structures, *Quarterly of applied mathematics* 45 (1987) 561–571.
- [22] Y. Saad, *Iterative Methods for Sparse Linear Systems*, 2nd Edition, Society for Industrial and Applied Mathematics, 2003.
- [23] A. C. Antoulas, *Approximation of Large-Scale Dynamical Systems*, *Advances in Design and Control*, SIAM, Philadelphia, 2005.
- [24] M. Powell, A hybrid method for nonlinear equations, *Numerical methods for nonlinear algebraic equations* 7 (1970) 87–114.

- [25] K. Madsen, H. B. Nielsen, O. Tingleff, *Methods for non-linear least squares problems* (2nd ed.) (2004).
- [26] E. Jones, T. Oliphant, P. Peterson, et al., *SciPy: Open source scientific tools for Python* (2001–).
- [27] J. J. Moré, B. S. Garbow, K. E. Hillstom, *User Guide for MINPACK-1*, Tech. Rep. ANL-80-74, Argonne National Laboratory, Argonne, IL, USA (Aug. 1980).
- [28] J. Ferziger, M. Perić, *Computational Methods for Fluid Dynamics*, 3rd Edition, Springer, Berlin, 2002.
- [29] G. Söderlind, The logarithmic norm. history and modern theory, *BIT Numerical Mathematics* 46 (3) (2006) 631–652.
- [30] J. Wild, Experimental investigation of Mach- and Reynolds-number dependencies of the stall behavior of 2-element and 3-element high-lift wing sections, in: *AIAA Paper 2012-0108*, 50th AIAA Aerospace Sciences Meeting including the New Horizons Forum and Aerospace Exposition, Nashville, TN, 2012.
- [31] T. Gerhold, O. Friedrich, J. Evans, M. Galle, Calculation of complex three-dimensional configurations employing the DLR-TAU-code, *AIAA paper 167*.
- [32] M. Galle, T. Gerhold, J. Evans, Parallel computation of turbulent flows around complex geometries on hybrid grids with the dlr-tau code, in: A. Ecer, D. Emerson (Eds.), *Proceedings of the 11th Parallel CFD Conference*, North Holland, Williamsburg, VA, 1999.
- [33] R. Pinnau, Model reduction via proper orthogonal decomposition, in: *Model Order Reduction: Theory, Research Aspects and Applications*, Springer, 2008, pp. 95–109.
- [34] R. Zimmermann, Towards best-practice guidelines for POD-based reduced order modeling of transonic flows, in: C. Poloni, D. Quagliare, J. Périaux, N. Gauger, K. Giannakoglou (Eds.), *Evolutionary and deterministic methods for design, optimization and control*, EUROGEN 2011, CIRA, Capua, Italy, 2011, pp. 326–341.
- [35] T. Bui-Thanh, M. Damodaran, K. Willcox, Proper orthogonal decomposition extensions for parametric applications in transonic aerodynamics, *AIAA Journal* 42 (8) (2004) 1505–1516.
- [36] A. Forrester, A. Sobester, A. Keane, *Engineering Design via Surrogate Modelling: A Practical Guide*, Wiley, 2008.